Research paper

Numerical investigation of the scour around a diamond- and square-shaped pile in a narrow channel

Mario Hurtado-Herrera [a], Miguel Uh Zapata [b], Abdelkader Hammouti [a,c], Damien Pham Van Bang [a,c,*], Wei Zhang [d], Kim Dan Nguyen [e]

[a] *Laboratory for Hydraulics and Environment, INRS-ETE, G1K 9A9 Québec, QC, Canada*
[b] *CONAHCYT – Centro de Investigación en Matemáticas A. C., CIMAT Unidad Mérida, PCTY, 97302, Mérida, Mexico*
[c] *Department of Civil and Environmental Engineering, ETS, Université du Québec, 1100 rue Notre Dame Ouest, Montreal, H3C 1K3, Québec, Canada*
[d] *Department of Civil Engineering, Xián Jiaotong-Liverpool University, 215123 Suzhou, China*
[e] *Laboratory for Hydraulics Saint Venant, Ecole des Ponts, EDF-CEREMA, 78400 Chatou, France*

ARTICLE INFO

ABSTRACT

In this paper, a numerical investigation is conducted to study the scour dynamics around vertical square- and diamond-shaped piles in clear-water and live-bed conditions. The focus is particularly on cases involving narrow channels, aiming to examine the differences compared to more extensively studied scenarios, such as wide channels with circular piles. This work employs a Large Eddy Simulation (LES) model to simulate the turbulent flows around the structures. The hydrodynamic model is based on the Navier–Stokes equations in σ-coordinate, and the bed evolution is simulated by solving the Exner-Polya equation. The governing equations are solved using a second-order unstructured finite-volume method. The model is initially validated through a comparison with experimental data and numerical results found in the literature. Subsequently, it is applied to conduct a comprehensive study, enhancing our understanding of the various conditions influencing the scour process. The results indicate that the shape of the piles has different effects on the scour depth under clear-water and live-bed conditions. In live-bed conditions, the simulations reveal a deeper scour around the square-shaped pile compared to the diamond-shaped pile at the equilibrium stage. Conversely, an opposite behavior is observed in clear-water conditions, with a deeper scour around the diamond pile. Moreover, this behavior is consistent across both narrow and wide channels. It is discovered that, in clear-water conditions, the evolution of the scour in a narrow channel reaches equilibrium faster than in a wide channel, leading to a deeper equilibrium scour hole in the wide channel scenario.

1. Introduction

A crucial aspect of infrastructure safety is the erosion of bed material near partially or fully submerged structures located offshore and along rivers and coastlines. These structures include vegetation, offshore wind turbines, and offshore piles. The erosion of bed material near bridge piles is a crucial factor in infrastructure safety, with 50% to 65% of bridge failures attributed to scour (Huber, 1991; Wardhana and Hadipriono, 2003; Lin et al., 2014; Taricska, 2014), highlighting its significant impact in similar structures. However, the local scouring around a pile leads to changes in flow behavior making this fluid–structure phenomenon challenging to model, including the formation of a horseshoe vortex (HSV) upstream of the pile, vortex shedding downstream, and lateral flow contraction (Raudkivi and Ettema, 1983; Roulund et al., 2005). Additionally, the complex flow behavior near a pile and the resulting scouring vary due to factors such as the flow

conditions, pile geometry, domain width, and sediment grain size, all but the last factor thoroughly investigated in this paper.

Scour is commonly studied under live-bed and clear-water conditions (Melville and Chiew, 1999). The resulting scour is known as in live-bed condition when sediment transport occurs throughout the channel, both with and without a structure. Conversely, in clear-water conditions, sediment transport is localized exclusively at the structure foundation and downstream of it (Melville and Chiew, 1999). Many studies have investigated the fluid–structured interaction of piles in channels. Most of these works focus on live-bed conditions commonly found in real-world scenarios. Nevertheless, we can find examples under clear-water conditions (Lachaussée, 2018; Stevens et al., 1991). For instance, while floods may lead to local scour in live-bed conditions at the base of the central piles of bridges, those located at the floodplain

---

can experience scour in clear-water conditions (Melville and Chiew, 1999).

Scour erosion tests are also influenced by the width of the channel. In the case of a circular pile, this relationship is often examined through the ratio D/W, known as the blockage ratio, where D represents the diameter of the pile and W denotes the width of the channel. Observations by Chen et al. (1995) suggest that for $D/W \geq 0.1$ in a circular pile, the transition to vortex shedding is delayed compared with a very low blockage ratio. Furthermore, the proximity between the lateral walls causes shear in the upcoming flow, leading to interactions between flow structures near the obstacle and the channel walls (Singha and Sinhamahapatra, 2010). Experimental studies, as presented by Mignot et al. (2015), indicate that the scour process is not influenced by the wall proximity as long as a fully developed flow separates the obstacle and the walls. Additionally, Lachaussée (2018) suggests that, in the clear-water conditions, $D/W \geq 0.1$ modifies the threshold velocity for the incipient formation and development of HSV in the scour hole.

The depth of scour upstream of the pier is well-known to depend on the strength of the HSV generated through the interaction between the flow and the pile. In particular, the role of pile geometry in this phenomenon cannot be neglected (Khosronejad et al., 2012). In recent years, there have been efforts to conduct numerical studies on the scouring process around non-circular piles. For example, Bordbar et al. (2021) examined square-shaped piles at various positions, focusing on high flow velocity and sediment conditions in a wide channel as presented by Roulund et al. (2005) on circular shape. He also addresses the influence of the geometry by studying the bluntness factor (BF), which is dependent on the pile geometry (Fleming et al., 1993). In contrast, Hurtado-Herrera et al. (2023) investigated a moderately low flow velocity in the clear water regime within a narrow channel as presented by Lachaussée (2018) on circular shaped piles. Yao et al. (2018) performed an experimental study featuring square- and diamond-shaped piles and determined the diamond-shaped pile as the optimal orientation to minimize scour over time, but focused their efforts in very high flow velocities representing live-bed scour or near live-bed scour. Bordbar et al. (2021) performed a numerical study of the scour around a circular-, square-, and diamond-shaped piles, concluding that, among the three piles, the diamond-shaped pile presents the least amount of scour and the square-shaped pile presents the most amount of scour. However, as Bordbar et al. (2021) also focuses in a high velocity flow in a wide channel, it is not clear if this observation holds for all cases.

In terms of pile geometry, the square- and diamond-shaped piles represent edge cases, with blunt factors BF→ ∞ and BF = 0, respectively (Fleming et al., 1993). Hence, these cases are of interest to further validate the predictive capabilities of the numerical model NSMP3D. Furthermore, the present paper contributes to fill in the research gap by proposing a numerical investigation into the effects of narrow and wide channels on the scouring process around square- and diamond-shaped piles in both clear-water and live-bed scour regimes. Notably, this work offers, to the best of the authors' knowledge, the first numerical analysis of square-shaped piles in both clear-water and live-bed conditions in a narrow and wide channel. To achieve this objective, the present paper proposes a computational model based on an in-house numerical model. The present model has been validated with notable success in the past for circular piles under low flow velocity in a narrow channel (Hurtado-Herrera et al., 2023) and high flow velocity in a wide channel (Zhang et al., 2020a). The numerical method employs a second-order unstructured finite-volume approach for solving the three-dimensional Navier–Stokes equations in σ-coordinates (Zhang et al., 2020b; Uh Zapata et al., 2023). Turbulence is modeled using a Large Eddy Simulation (LES) method. Bed evolution is simulated through the Exner-Polya equation for non-cohesive sediment, incorporating the Engelund and Fredsøe model (Engelund and Fredsøe, 1976).

The present paper is structured as follows. Section 2 provides a detailed explanation of the mathematical model for fluid flow and the sediment bed. Section 3 describes the numerical model, including information about the computational domain and mesh resolution. Section 4 focuses on validating the present model against experimental data and numerical results found in the literature. The primary findings of this work are covered in Section 5. This section presents a comparative analysis of the scour process and hydrodynamics in different cases, with the cylinder case serving as a point of reference for the final results. Finally, Section 6 presents the conclusions and future work.

2. Governing equations

This paper uses Large-Eddy Simulation (LES) for the hydrodynamic model, chosen for its suitability in handling flows around structures (Hurtado-Herrera et al., 2023; Zhang et al., 2020a,b). On the other hand, this study specifically centers on sediment transport, where suspended sediment can be negligible. As a result, the investigation only considers the bedload formulation through the Exner-Polya equation.

2.1. Hydrodynamic model

Instead of resolving all turbulent scales (as in Direct Numerical Simulation or DNS), LES applies a spatial filter to distinguish larger turbulent motions, explicitly resolved, from the smaller, unresolved scales that it models separately. The filtered Navier–Stokes equations are:

$$\frac{\partial \bar{u}_i}{\partial t} + \frac{\partial \bar{u}_i \bar{u}_j}{\partial x_j} = -\frac{1}{\rho}\frac{\partial \bar{p}}{\partial x_i} + \frac{\partial}{\partial x_j}\left[\nu\left(\frac{\partial \bar{u}_i}{\partial x_j} + \frac{\partial \bar{u}_i}{\partial x_i}\right)\right] - \frac{\partial \tau_{ij}}{\partial x_j} + f_i, \tag{1}$$

$$\frac{\partial \bar{u}_i}{\partial x_i} = 0, \tag{2}$$

where x_i ($i = 1, 2, 3$) is the ith Cartesian coordinate, $\bar{u}_i$ denotes the ith velocity component, represents $\bar{p}$ the pressure, ρ stands for the density, ν is the kinematic viscosity, f_i is an external force, and τ_{ij} is a sub-grid stress (SGS) tensor needed to take into account unresolved length scales. In this paper, the SGS tensor is modeled by

$$\tau_{ij} = 2\nu_t \overline{S}_{ij} + \frac{1}{3}\tau_{jj}\delta_{ij}, \tag{3}$$

where δ_{ij} is the Kronecker delta, ν_t is the sub-grid scale turbulent viscosity, and $\overline{S}_{ij}$ is the rate-of-strain tensor for the resolved scale given by

$$\overline{S}_{ij} = \frac{1}{2}\left(\frac{\partial \bar{u}_i}{\partial x_j} + \frac{\partial \bar{u}_j}{\partial x_i}\right) \tag{4}$$

Using the Smagorinsky model, the eddy viscosity is modeled as follows:

$$\nu_t = L_s^2 |\bar{S}|, \tag{5}$$

where $|\bar{S}| = \sqrt{2\bar{S}_{ij}\bar{S}_{ij}}$ and L_s is the sub-grid length scale. This length scale does not maintain a constant value within the near-wall region; rather, it diminishes as it gets closer to the wall. This boundary layer effect is captured by the Mason-wall matching power (Mason and Thomson, 1992):

$$\frac{1}{L_s^2} = \frac{1}{(C_s \Delta)^2} + \frac{1}{(\kappa L_w)^2}. \tag{6}$$

Here, $C_s = 0.1$ is the Smagorinsky constant, Δ is the average spacing $\Delta = V^{1/3}$ per cell volume V, κ is the Von Kármán constant, and L_w is the distance from the cell center of a control volume to the wall.

Finally, this work employs non-dimensional equations using the diameter of the pile, D, and the mean flow velocity, U, as reference scales for the length and velocity, respectively. This selection of reference scales, allows the governing equations to be expressed in terms of the Reynolds number

$$\text{Re}_D = \frac{UD}{\nu}, \tag{7}$$

which is based on the cylinder diameter, the mean flow velocity, and kinematic viscosity.

2.2. Morphodynamic model

The present model assumes a mobile bed consisting of non-cohesive sediment. The morphological evolution of such sediment bed is described by the Exner-Polya equation:

$$(1 - \eta)\frac{\partial z_b}{\partial t} + \frac{\partial q_{b_i}}{\partial x_i} = 0, \tag{8}$$

where $\eta = 0.4$ is the porosity of the bed, z_b is the bed elevation, and $q_{b_1 i}$ $(i = 1, 2)$ is the bedload transport rate given by the formula proposed by Engelund and Fredsøe (1976):

$$q_{b_i} = \frac{\pi d}{6} p_{EF} u_{bi}, \tag{9}$$

where d is the particle diameter, p_{EF} is the percentage of particles in motion modeled, and u_{b_i} are the mean velocity components of a sediment particle in movement. The value p_{EF} is given by

$$p_{EF} = \begin{cases} \left[1 + \left(\frac{\pi \mu_d}{6(\theta - \theta_c)} \right)^4 \right]^{-\frac{1}{4}} & , \quad \theta > \theta_c \\ 0 & , \quad \theta \le \theta_c. \end{cases} \tag{10}$$

Here, μ_d is the dynamic friction coefficient, θ is the Shields number, and θ_c is its critical value for the initiation of motion. The mean velocity is calculated as follows:

$$u_{b_i} = a \left(1 - 0.7\sqrt{\frac{\theta_c}{\theta}} \right) u_{\tau_i}, \tag{11}$$

where a is an empirical constant and u_τ is the friction velocity. As implemented by Zhang et al. (2020a), θ_c is taken as

$$\theta_c = \theta_{c_0} \left(\cos \beta \sqrt{1 - \frac{\sin^2 \alpha \tan^2 \beta}{\mu_s^2}} - \frac{\cos \alpha \sin \beta}{\mu_s} \right), \tag{12}$$

where θ_{c_0} is the critical Shields number for the initiation of motion in a bed with slope zero, μ_s is the static friction coefficient, β is the maximum angle of repose, and α is the difference between the angle of the flow near the bed and the maximum angle of repose β.

The critical Shields number θ_{c0} can be estimated by the formula proposed by Soulsby and Whitehouse (1997):

$$\theta_{c0} = \frac{0.3}{1 + 1.2D^*} + 0.055 \left(1 - e^{-0.02D^*} \right), \tag{13}$$

where

$$D^* = \left(\frac{(\rho_s/\rho_w - 1)g d^3}{\nu^2} \right)^{1/3}, \tag{14}$$

where ρ_s is the density of the sediment and ρ_w is the density of the fluid.

The friction velocity is calculated by the method developed by Nikuradse (1933):

$$\frac{u}{u_\tau} = \kappa^{-1} \ln \left(\frac{z}{z_0} \right), \tag{15}$$

where κ is the Von Kármán constant, and z_0 is the distance from the boundary at which point the idealized velocity given by the Wall Law goes to zero. In this paper, this value is governed by the friction Reynolds number

$$\text{Re}_\tau = \frac{u_\tau k_s}{\nu}, \tag{16}$$

with k_s being the Nikuradse sand roughness. Based on Re_τ, three hydraulic regimes are defined to compute z_0. The flow is hydraulically smooth for $\text{Re}_\tau \le 5$, and rough for $\text{Re}_\tau \ge 70$. Soulsby (1997) developed the following transitional formula to link both regimes:

$$z_0 = \frac{\nu}{9 u_\tau} + \frac{k_s}{30} \left[1 - \exp\left(-\frac{u_\tau k_s}{27 \nu} \right) \right]. \tag{17}$$

To prevent bed slopes from exceeding the physical angle of repose, this study incorporates a sand-slide model in addition to the morphodynamic model (8)–(17). The method utilizes the mass-conservation-based algorithm developed by Khosronejad et al. (2012). The elevation gradient between a given site and the neighboring horizontal cell center is used to calculate the bed slope. A corrective measure is taken to adjust the bed elevation if this slope exceeds the maximum angle of repose for the material. By using the area projection of the cells, these bed adjustments are calculated using mass conservation principles. Furthermore, this causes the mesh points to shift exclusively vertically, resulting in no change to the cell area. More details about this algorithm in a triangular mesh can be found in Zhang et al. (2020a).

3. Numerical model

Discretization issues may arise due to the inconstant bathymetry induced by the mobile bed. This is prevented by mapping the vertical coordinate onto a set range, $\sigma = [0, 1]$, thereby simplifying the geometry of the domain. The σ-transformation is defined as:

$$t^* = t, \ x^* = x, \ y^* = y, \ \sigma = \frac{z + h}{h}; \tag{18}$$

where $z \in [-h, 0]$, $h = h_0 - z_b$, and h_0 is the initial water depth. The use of the σ-transformation ensures a two-way coupling of hte hydrodynamic and morphodynamic models. More details can be found in Zhang et al. (2020b)

In the present work, the hydrodynamics and morphodynamics of the problem are computed using the *Three-dimensional Navier–Stokes Multiphase Flow* (NSMP3D) research code as the computational model. NSMP3D is a second-order finite-volume numerical model in both time and space, specifically designed to solve the incompressible equations in σ-coordinates across unstructured mesh grids. A Crank–Nicholson scheme is used for the temporal discretization, and the projection method is used to decouple the pressure and velocity field. The Successive Over-relaxation Method is used to solve the resulting linear systems. The entire program operates in parallel through the Message Passing Interface (MPI).

All simulations were performed utilizing the computational cluster provided by the Digital Research Alliance of Canada. Depending on mesh size and performance, each simulation used between 2 and 4 nodes. The specifications for a single node are 2009 GB of memory, 2 x AMD Rome 7532 @ 2.40 GHz 256M, cache L3, totaling 64 cores. Computational time varied between 125.7 h and 283 h. For a comprehensive understanding of this numerical model, detailed descriptions can be found in previous studies with various turbulent validation cases (Uh Zapata and Pham Van Bang, 2016; Uh Zapata et al., 2014; Zapata et al., 2019; Uh Zapata et al., 2023).

3.1. Computational domain and boundary conditions

This paper investigates the impact on the scouring process around piles by varying the computational domain width, denoted as W, and experimenting with circular and square-shaped pile geometries. Here, the pile diameter D is defined as the pile diameter in the case of a circular pile and the side length in the case of a square-shaped pile.

In all scenarios, the inlet boundary conditions are defined by a constant flow velocity determined using the Swamee profile (Swamee, 1993). For the outlet, non-reflective boundary conditions are employed. Slip boundary conditions are implemented on the top surface, while non-slip boundary conditions are applied to the bottom bed. At the lateral walls, non-slip conditions are applied for the narrow channel, while slip conditions are employed for the wide channel. The geometry of the computational domain with boundaries is illustrated in Fig. 1.

Two geometrical domains are designed to simulate both a narrow and a wide channel. In the case of the narrow channel, the numerical domain closely reproduces the experimental setup presented by Lachaussée et al. (2018). Consequently, the numerical domain is
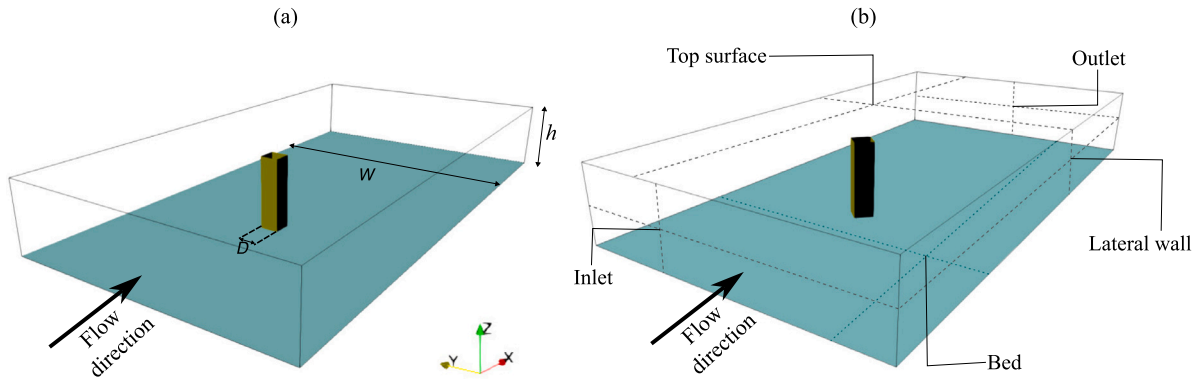
Fig. 1. Set-up for the (a) square- and (b) diamond-shaped piles.

given by a plume with a width of $W = 8D$. Numerical boundaries are established at the inlet and outlet, positioned $10D$ upstream and $20D$ downstream of the pile's center, respectively. In the case of the wide channel, the width of the computational domain is increased to $W = 16D$. This is a choice made to further mitigate any potential impact these boundaries might have on the flow near the obstacle. In all test cases, the initial water depth is consistently set to $h = 4D$.

Simulations are conducted in both narrow and wide channels, exploring clear-water and live-bed conditions for both a cylindrical pile and a square-shaped pile. The square-shaped pile is tested at two different orientations. In the square configuration, one face of the pile was positioned normal to the inlet flow. Thus, the projected pile width under steady current flow coincides with the side of the square ($w_p = D$). On the other hand, in the diamond configuration, the inlet flow aligned parallel to one of the diagonals of the square base of the pile. As a result, the projected pile width coincides with the diagonal of the square and is given by $w_p = \sqrt{2}D$.

3.2. Mesh grid

For the numerical results presented in Section 5, the three-dimensional mesh is constructed with prism-shaped cells arranged in vertical columns, collectively forming a non-structured triangular mesh. For instance, Fig. 2 provides a detailed horizontal view of the mesh characteristics employed in this study for the diamond-shaped pile for both narrow and wide channels. It is important to note that we maintain a consistent distribution of triangles for both type of channels to prevent any divergent behaviors arising from variations in the mesh near the pile. For all cases, the maximum length of the triangle sides, denoted as Δx, is set to $\Delta x = 0.125D$ away from the obstacle. On the wake side of the obstacle, the horizontal resolution is reduced, with an average of $\Delta x = 0.05D$. In close proximity to the obstacle, the finest resolution is achieved, with $\Delta x = 0.015D$.

Fig. 3 shows a closer examination of the mesh around the pile for the different geometries investigated in this paper. Additional information regarding these values is available in Table 1. On the other hand, in the vertical direction, the 96 layers are arranged in a progressive order, ensuring that the minimum height at the bottom of the domain remains consistent at $\Delta z = 0.01D$ across all scenarios.

The following section focuses on validating the proposed numerical method under different flow conditions, different pile geometry, and different blockage ratios. The domain size and mesh resolution are modified for these cases to match the experimental setup. Specific information about the discretization in each case is provided; however, the general triangular distribution is similar to the ones described in this section.

Table 1
Details on the horizontal mesh grid used for all test cases.

Mesh	Pile shape	Channel type	Elements	Vertices	min Δx	max Δx
Mesh 1	Circular	Narrow	51,653	26,233	0.015D	0.125D
Mesh 2	Circular	Wide	85,193	43,067	0.015D	0.125D
Mesh 3	Square	Narrow	60,140	30,474	0.020D	0.125D
Mesh 4	Square	Wide	98,450	49,693	0.020D	0.125D
Mesh 5	Diamond	Narrow	67,372	34,090	0.020D	0.125D
Mesh 6	Diamond	Wide	100,784	50,860	0.020D	0.125D

4. Comparison between experiment and simulation

The numerical simulations in this section are devoted to demonstrate the capability of the present model in accurately predicting the flow and scour processes around obstacles with different geometries. The present model's robustness is validated against experimental data from three different cases. Initially, numerical simulations are performed to replicate live-bed conditions as reported by Roulund et al. (2005), focusing only on a circular pile in a wide channel. Subsequently, we examine the test conducted by Lachaussée (2018) under clear-water conditions, both with and without a circular pile in a narrow channel. Finally, the model is validated using square- and diamond-shaped piles in clear water conditions in a narrow channel against the experimental data documented by Khosronejad et al. (2012). In the last case the critical Shields number was not explicitly provided in Khosronejad et al. (2012), so it was estimated to be $\theta_{c0} = 3.03 \times 10^{-2}$ using Eq. (13). It is noteworthy that all computations were stopped based on data availability rather than meeting an equilibrium criterion. A complete list of parameters for the experimental setup in all three cases is provided in Table 2.

4.1. Example 1: Circular pile in a wide channel under live-bed conditions

In the first example, we verify the method's capability to simulate the scour process in live-bed conditions for a circular pile in a wide channel, following the specifications outlined by Roulund et al. (2005) and provided in Table 2. In this test, the computational domain has dimensions $30D \times 16D$. In this case, the horizontal mesh comprises 85,193 triangular elements with a maximum and minimum side lengths of $\Delta x = 0.125D$ and $\Delta x = 0.015D$ located far and close to the pile, respectively. The number of layers was set as 96 layers, and the first cell center near the bed has a distance to the bed of $\Delta z = 0.01D$ resulting in $z_+ = 19.2$ wall units.

The bed shear stress is directly related to the erosive capacity of the flow and influences sediment scour around the circular pile. As this parameter plays a crucial role in the scour process, it is important to be properly simulated by our numerical model. Fig. 4 shows the bed shear stress amplification as reported in Roulund et al. (2005) for the rigid rough bed case, comparing it with the simulation results from our
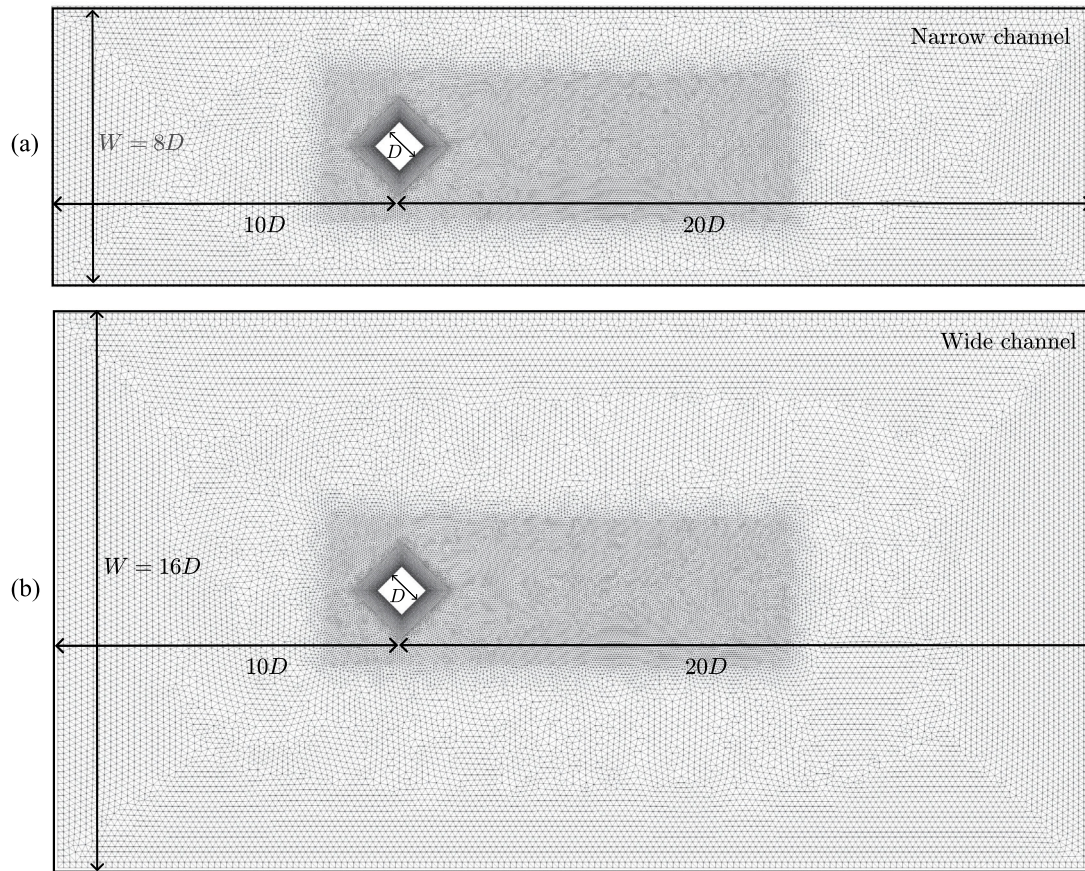
Fig. 2. Horizontal mesh for the narrow and a wide channel with a diamond-shaped pile used in the numerical simulations.
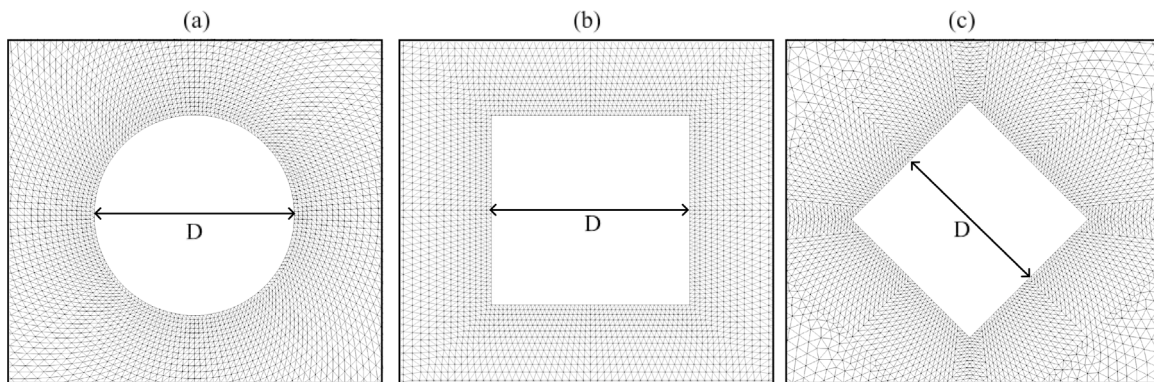

Fig. 3. Details on the horizontal triangular mesh distribution close to the (a) circular, (b) square-shaped and (b) diamond-shaped piles.

present model. The shear stress amplification is defined as the ratio τ/τ_∞, where τ is the shear stress magnitude and τ_∞ is the shear stress produced by the unperturbed flow. The model agrees convincingly with the findings of Roulund et al. (2005), particularly concerning the location of the maximum shear stress relative to the pile's center, which results from the contraction of the flow lines.

The proposed model was also evaluated against experimental and numerical data from Roulund et al. (2005) for scouring around a circular pile in live-bed conditions. Fig. 4(b) illustrates the temporal evolution of the non-dimensional scour depth (S/D) upstream of the pile. During the initial stages of scour, Roulund's numerical model exhibits a slight tendency to over-predict the depth on the upstream side. In contrast, the present model shows a minor underestimation compared to the experimental data. It is noteworthy that, in general, the present numerical results demonstrate a closer agreement with the experimental findings than the numerical model provided by Roulund's model.

4.2. Example 2: Circular pile in a narrow channel under clear-water conditions

For the second example, we investigate the scour process in the clear-water regime for a circular pile and a narrow channel, as detailed in Lachaussée (2018). The parameters of this example are also described in Table 2. Lachaussée performed a set of experiments in two steps.

Table 2
Parameters of the experimental tests used as reference to validate the numerical simulations of the present model.

Experiment	Lachaussée (2018) Rigid bed Without pile	Lachaussée (2018) Mobile bed Circular	Khosronejad et al. (2012) Mobile bed Square	Khosronejad et al. (2012) Mobile bed Diamond	Roulund et al. (2005) Rigid bed Circular	Roulund et al. (2005) Mobile bed Circular
Pile diameter D (m)	–	0.010	0.165	0.165	0.100	0.100
Flume width W (m)	0.100	0.100	1.210	1.210	2.000	1.800
Water depth h (m)	0.160	0.160	0.139	0.160	0.200	0.200
Mean grain diameter d (mm)	–	0.270	0.850	0.850	–	0.260
Equivalent sand roughness k_s (mm)	0.675	0.675	2.125	2.125	0.650	0.650
Mean flow velocity U (m/s)	0.160	0.160	0.220	0.210	0.460	0.460
Inflow friction velocity u_τ (m/s)	9.10×10^{-3}	9.87×10^{-3}	1.04×10^{-2}	9.87×10^{-3}	1.80×10^{-2}	1.80×10^{-2}
Reynolds number $\mathrm{Re} = Uh/\nu$	2.56×10^4	2.56×10^4	3.06×10^4	3.29×10^4	9.20×10^4	9.20×10^4
Pile Reynolds number $\mathrm{Re}_D = UD/\nu$	–	1.60×10^3	3.63×10^4	3.47×10^4	4.60×10^4	4.60×10^4
Froude number $Fr = U/\sqrt{gh}$	0.150	0.150	0.190	0.170	0.330	0.330
Critical Shields number θ_{c0}	4.04×10^{-2}	4.04×10^{-2}	3.03×10^{-2}	3.03×10^{-2}	4.08×10^{-2}	4.08×10^{-2}
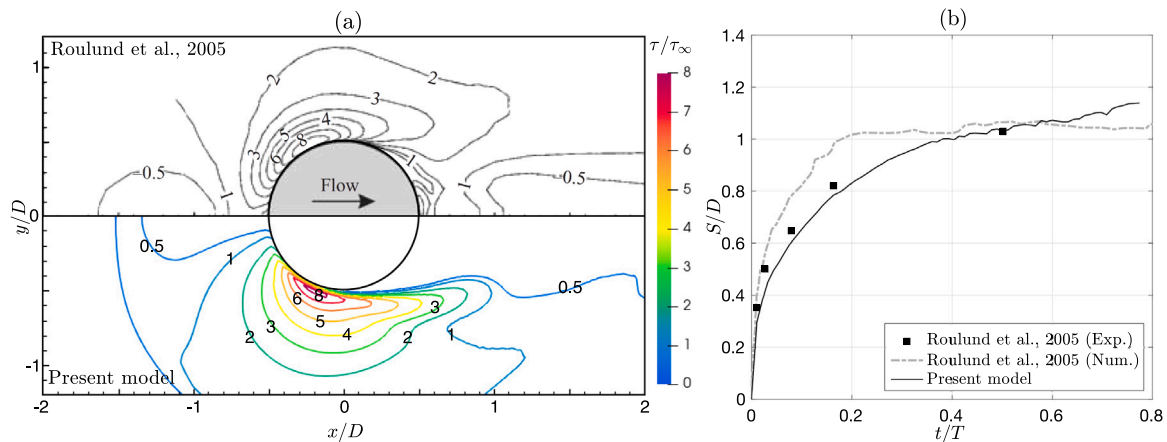
Fig. 4. (a) Bed shear stress amplification τ/τ_∞ for the rigid rough bed case at $Re_D = 46000$, comparing results from Roulund et al. (2005) with those obtained from the present model. (b) Time evolution of the scour depth S/D for the circular pile in live-bed conditions. The time scale is defined by $T = D^2(g(s-1)d^3)^{-1/2}$ (Sumer et al., 1992).

Following the experimental setup, the computational domain is $30D$ long and $10D$ wide. The center of the pile is positioned $10D$ downstream of the inlet. The height of the domain is set as $h = 8D$. In this case, the horizontal mesh has 12,077 triangular elements of varying sizes. The average side lengths are set to $\Delta x = 0.25D$ and $\Delta x = 0.015D$ far and close to the pile, respectively. In the vertical direction, the grid consists of 96 layers. The first cell center near the bed has a distance to the bed of $\Delta z = 0.02D$, equivalent to $z_+ = 2.82$ wall units.

Fig. 5 provides a comparison of different horizontal profiles of bed topography (z_b) between the experimental data from Lachaussée (2018) and our numerical simulations at $t = 2.4$ hours. Fig. 5(a) presents the comparison along the plane $y/D = 0$. It is notable that, although the scour hole is slightly deeper in the numerical simulation, the bed topography is well described by the model, specially the dune position. Figs. 5(b) and (c) show a good agreement between the bed topography near the pile and the numerical results, with some discrepancy observed farther from the obstacle. This inconsistency can be attributed to the limitations of the measurement method, as noted in Lachaussée (2018), where variations of up to 1 mm from the initial bed position cannot be precisely measured. Further details regarding the validation of this case are available in Hurtado-Herrera et al. (2023).

4.3. Example 3: Square-shape pile in a narrow channel under clear-water conditions

The third example aims to validate the model's capabilities in predicting the scour process around a square- and diamond-shaped pile situated in a narrow channel under clear-water conditions. The numerical simulations are compared with experimental results provided by Khosronejad et al. (2012). The experimental setup involves a square-shaped pile with a side length of $D = 0.165$ m, positioned in two distinct orientations to represent square and diamond piles. A comprehensive list of parameters is available in Table 2.

Following the experimental setup, the numerical simulations are conducted in a computational domain that is $35D$ long and $7.25D$ wide. The center of the pile is positioned $15D$ downstream of the inlet. The height of the domain is set equal to the water depth in each case, with values of $h = 0.842D$ and $0.951D$ for the square and diamond configurations, respectively. In this case, the horizontal unstructured grid has 44,392 triangular elements of varying sizes. The average side lengths are set to $\Delta x = 0.125D$ and $\Delta x = 0.02D$ far and close to the pile, respectively. For the diamond configuration, the numerical grid consists of 43,560 elements in the horizontal direction, with $\Delta x = 0.125D$ far from the pile and $\Delta x = 0.014D$ close to the pile. In the vertical direction,
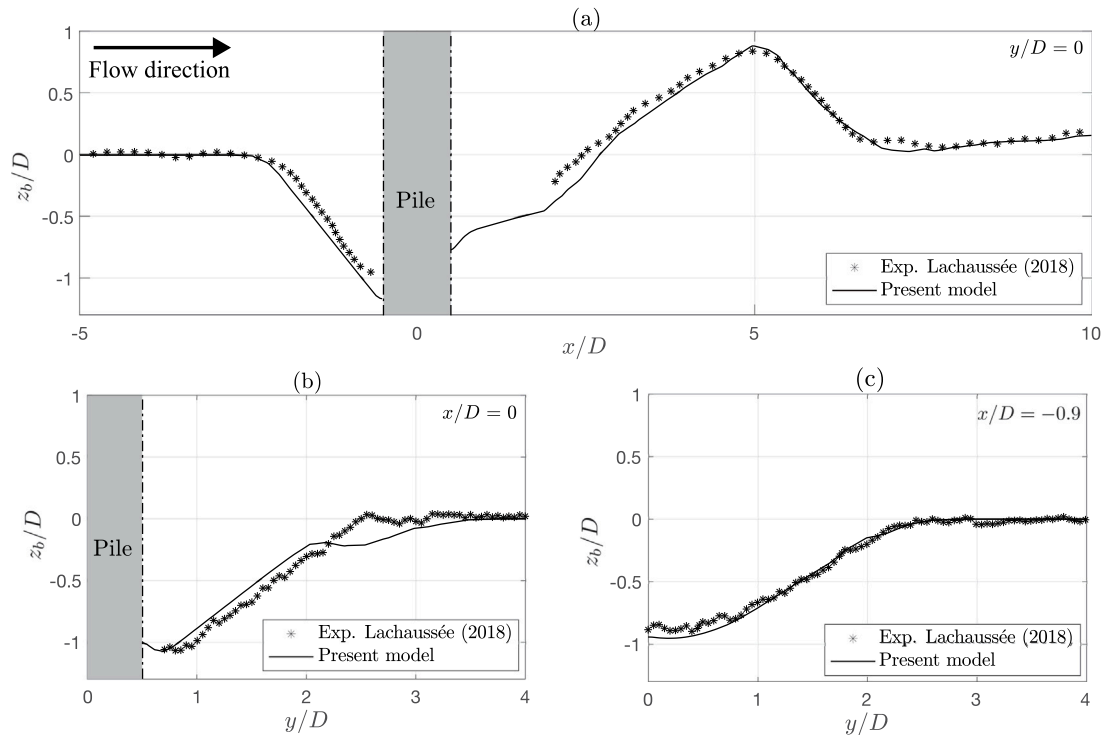
Fig. 5. Comparison of the bed topography at $t = 2.4$ hours between numerical results and experimental data reported in Lachaussée (2018): (a) Streamwise profile at $y = 0$, (b) Transversal profile at $x = 0$, and (c) Transversal profile at $x = -9$ mm.

the grid consists of 96 layers. The first cell center near the bed has a distance to the bed of $\Delta z = 0.025 D$, equivalent to $z_+ = 4.07$ for the square and $z_+ = 3.8$ for the diamond, both measured in wall units.

Fig. 6 compares the bed topography at the simulations' equilibrium scour with Khosronejad et al. (2012)'s experimental results. The results are in good agreement in both the magnitude of the scour depth and the height of the dune for the square pile scenario (Fig. 6a), and it correctly predicts the location with scour depth. For the diamond pile case (Fig. 6b), the magnitude of the maximum scour depth is in good agreement with the experimental data, but it predicts the location of the maximum scour depth upstream rather than lateral to the pile. The model was able to capture the scour behavior upstream and lateral to the pile. However, it failed to accurately predict the deposition in the wake zone of the domain. The different processes occurring upstream and downstream of the pile could account for this mismatch. Flow stagnation in front of the obstacle induces a vertical downflow impingement to the sediment bed and vortex in the wake region a vertical upflow sucking sediment from the bed. Both phenomena are explained in Zhang et al. (2020a) in detail, and are also observed during the simulation on square- and diamond-shaped obstacle. The current version can correctly predict the erosion crater, but need further improvement for the vertical ascending suspended sediment. It is also noteworthy that the bed elevation pattern was measured using laser profilometry after the flow was stopped in the experiments. This measurement method may affect the erosion pattern in the region with sharp elevation gradient. Therefore, we do not expect a perfect reproduction of the bed topography in the wake zone for the numerical results.

Fig. 7 compares the experimental and numerical results reported in Khosronejad et al. (2012), the numerical results reported in Bordbar et al. (2021), and the numerical results of the present model. It is noteworthy that although the physical model matches narrow channel conditions, the simulations conducted in Khosronejad et al. (2012) and Bordbar et al. (2021) use a wide channel configuration. To account for potential impacts of wall proximity on the experimental results described in Khosronejad et al. (2012), we use a narrow channel
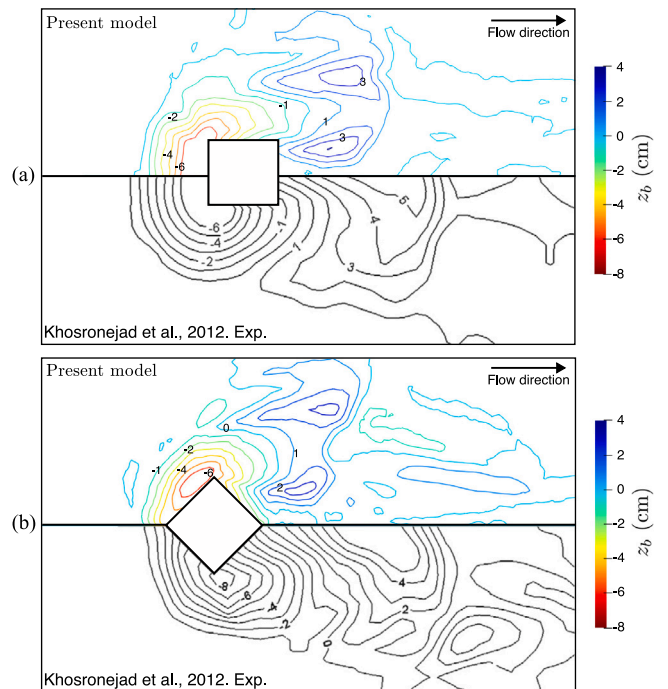

Fig. 6. Numerical and experimental results (Khosronejad et al., 2012) of the bed topography at the equilibrium for the square and diamond case.

arrangement in this work. The scour depth progression for the square-shaped pile scenario is well captured by the current model, as shown in Fig. 7(a). Fig. 7(b) illustrates how all three numerical models underestimate the scour depth at the start of the simulation in the diamond pile scenario. Later in time, nevertheless, the current model gets a better agreement with the measurements.
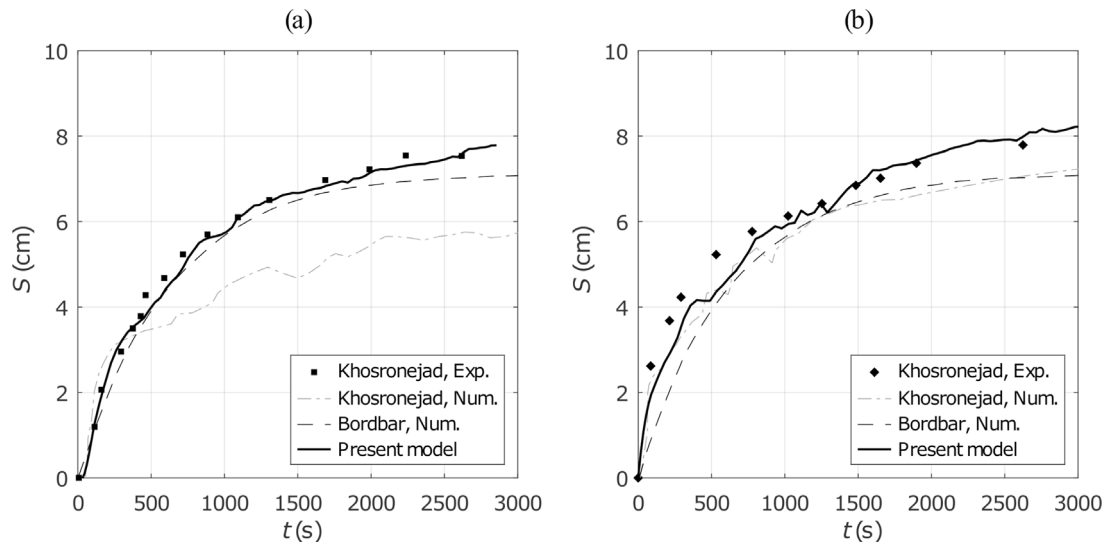
Fig. 7. Time evolution of the scour depth for the (a) square-shaped and (b) diamond-shaped pile case.

5. Results and discussion on square- and diamond-shaped pile

In this section, we present outcomes on square- and diamond-shaped piles. In particular we detail the effect of the channel width and the flow regime on the erosional pattern and scour dynamics. Specifically, we aim to investigate cases involving narrow channels and square- and diamond-shaped piles at different orientations and examine how they differ from more extensively studied scenarios, such as wide channels with circular piles. Thus, the parameters in our simulations are configured to yield the following two different cases:

- *Clear-water conditions.* The first regime corresponds to a slow flow with $D = 0.02$ m and $U = 0.15$ m/s, yielding an approximate Reynolds number of $\mathrm{Re}_D = 2700$. It results in a sub-critical friction velocity (i.e friction velocity u_τ lower than the sediment critical value for erosion) $u_\tau = 7.3 \times 10^{-3}$. Therefore, this test falls within the clear-water regime.
- *Live-bed conditions.* The second regime corresponds to a rapid flow with $D = 0.1$ m and $U = 0.46$ m/s, yielding an approximate Reynolds number of $\mathrm{Re}_D = 46000$. It results in a super-critical friction velocity $u_\tau = 1.828 \times 10^{-2}$, ensuring live-bed conditions.

As described in Fig. 3, in the case of narrow channels, we adopt a computational width of $W = 8D$. The lateral walls have no-slip boundary conditions to simulate physical walls. To simulate a wide channel, the computational domain's width is doubled, $W = 16D$, and the lateral walls have slip boundary conditions.

5.1. Flow dynamics around square- and diamond-shape piles

This section analyzes the hydrodynamic properties of the flow for the square and diamond-shaped piles. Specifically, for the narrow domain with a square-pile, a blockage ratio of $D/W = 0.125$ is defined, as the pile's projected width is $w_p = D$. This ratio, combined with the application of no-slip boundary conditions at the lateral walls, defines conditions characteristic of a narrow-channel configuration. On the other hand, for the wide domain, a blockage ratio of $D/W = 0.0625$ is utilized. Complemented by slip conditions at the lateral walls, this configuration establishes open-channel flow conditions. For the diamond-shape pile, the blockage ratio is slightly increased as the projected width of the pile aligns with the diagonal of the square, resulting in approximately $w_p = 1.414D$.

Fig. 8 shows the Q-criterion to showcase the vortices (horseshoe and shedding) around the square and diamond piers under clear-water conditions. The Q-criterion was computed in post-processing. In the square

results, a separation vortex starts forming from the lateral corners of the lee-side face of the pile. In the diamond results, the separation vortex starts forming at the lateral vertices of the pile. This remark aligns with the vortex behavior documented by Bordbar et al. (2021). On the other hand, the HSV exhibits similar qualitative characteristics for both square- and diamond-shaped piles. However, the narrow-channel configuration restricts the extension of the HSV along the spanwise direction. Additionally, in the narrow channel, there are extra vortex structures along the lateral walls, arising from the interaction between the HSV and the wake with the channel walls.

The vorticial structures near and downstream of the pile are directly influenced by the domain geometry and the flow velocity. As illustrated in Fig. 8, the wake vortices downstream of the pile, as well as the HSV, are different in lateral and longitudinal expanses depending on the pile shape, channel width, and flow velocity. However, the characteristics such as size, shape, and distance from the pile of the HSV seem to be more strongly governed by the flow velocity and the geometric features of the pile. Fig. 9 displays the streamlines of the flow field for both square- and diamond-shaped piles configurations, utilizing the wide channel under both clear-water and live-bed conditions. The streamlines are presented in the vertical plane at $y = 0$, aligned with the stagnation point. In both conditions, the HSV upstream of the pile is located farther from the nose of the square compared to the nose of the diamond.

Note that in Fig. 9, the model predicts a small HSV rotating counter-clockwise for only the square-shaped pile (not in the diamond) in addition to the main HSV system, observed in both clear water and live-bed conditions. This behavior can be explained by examining the bluntness factor (BF), as defined in Fleming et al. (1993), and the average vortex stretching rate VS from the nose to the maximum thickness of the obstacle given by Simpson (1995):

$$VS = 10^b (BF)^m, \tag{19}$$

where $b = 0.0482$ and $m = 0.8816$. The bluntness factors for the circular, square-shape and diamond-shaped piles are $BF = 1.1$, $BF \rightarrow \infty$ and $BF = 0$, respectively. Thus, the diamond bluntness factor indicates that, theoretically, the HSV should stretch from the nose to the maximum thickness at a rate $VS = 0$. This aligns with the model predictions, as no HSV is observed at the nose of the pile.

Next, numerical results of the flow are analyzed by comparing the friction velocity amplification, defined as $u_\tau/u_{\tau_{crit}}$. Here, we have $u_{\tau_{crit}} = 1.27 \times 10^{-2}$ m/s for the piles under both clear-water and live-bed conditions. We begin our analysis by focusing on the clear-water
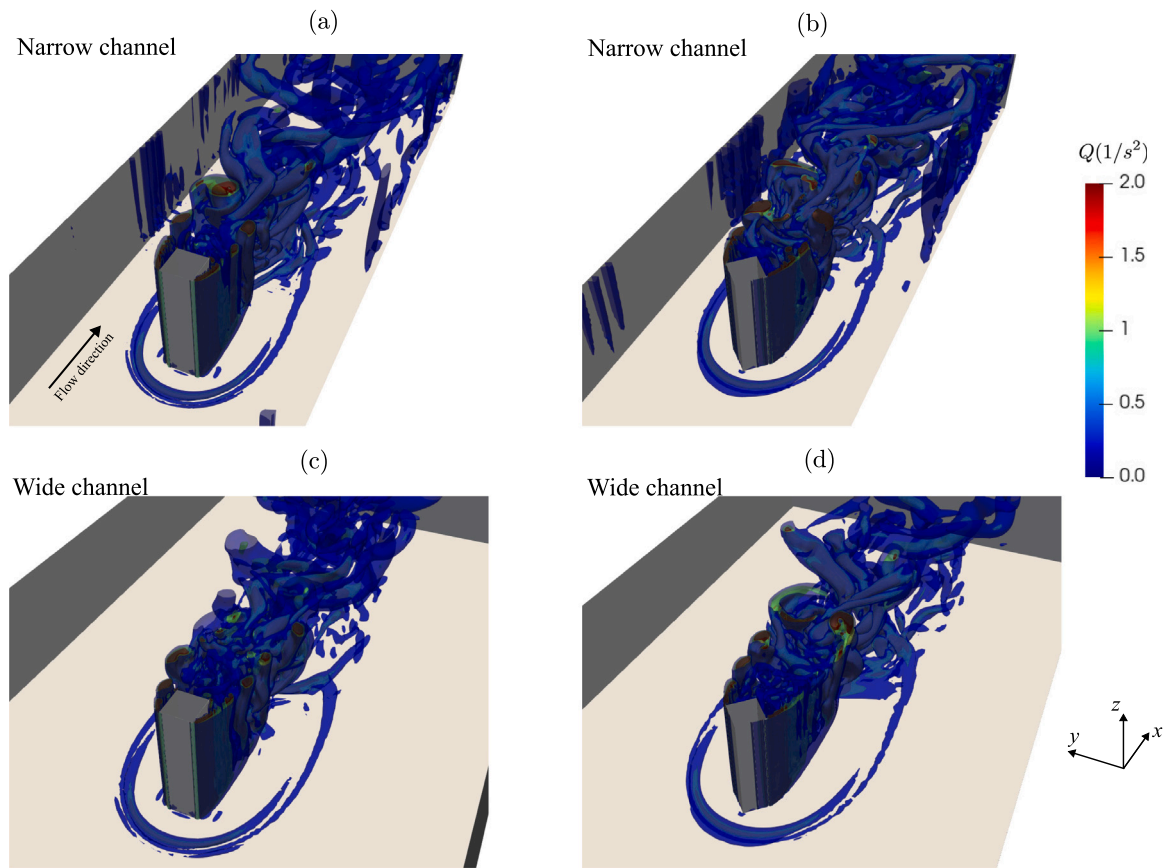
Fig. 8. Vortex structures around the square- and diamond-shaped piles using a narrow and a wide channel.
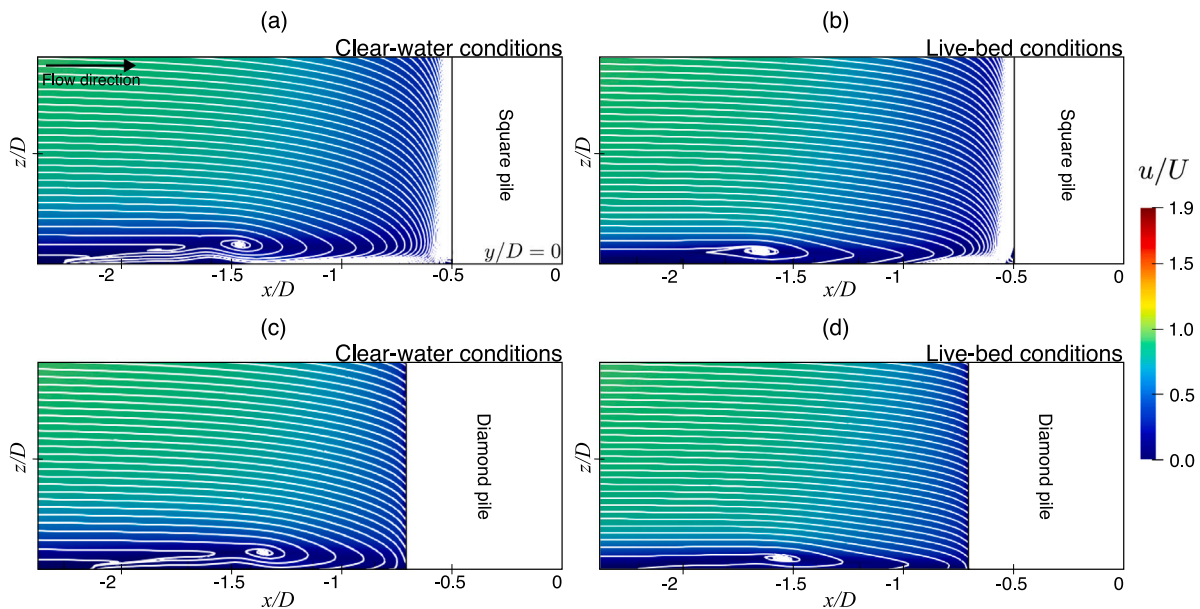

Fig. 9. Streamlines of the HSV system upstream of the square- and diamond-shaped pile in clear-water and live-bed conditions for the wide channel.

conditions. Fig. 10 illustrates the results for both square configurations under this regime. As expected, we can see that the diamond shape is more streamlined than the square, leading to a deviation in the flow pattern. The separated flow around the square reattaches at the center line in a manner similar to a backfacing step. However, for the diamond shape, the reattachment length is longer, indicating a distinct flow behavior. Additionally, due to the larger blockage ratio in the narrow

channel configuration, there is an amplification of the flow contraction relative to the wide channel cases.

The intensity of the mean HSV forming upstream of the piles is one of the main factors influencing the development of local scour. In the simulations presented in Fig. 10, the region where the threshold for sediment motion is overshoot lies within the boundaries of the horseshoe vortex. Moreover, this region of sediment motion significantly differs
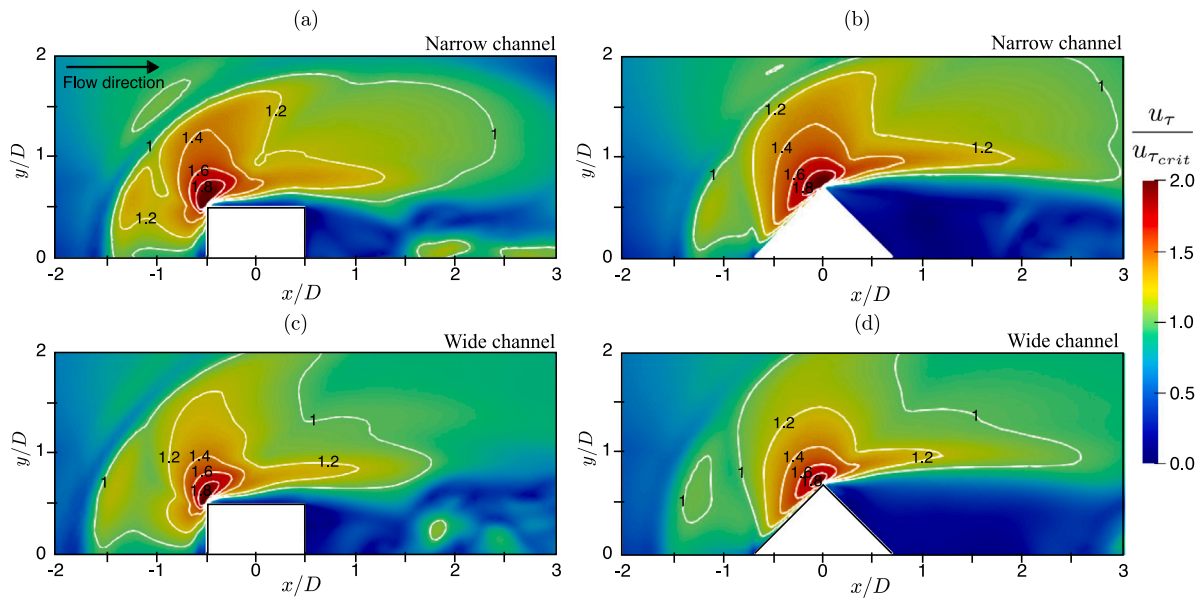
Fig. 10. Friction velocity amplification $u_\tau/u_{\tau_{crit}}$ over a rigid bed for clear-water conditions.
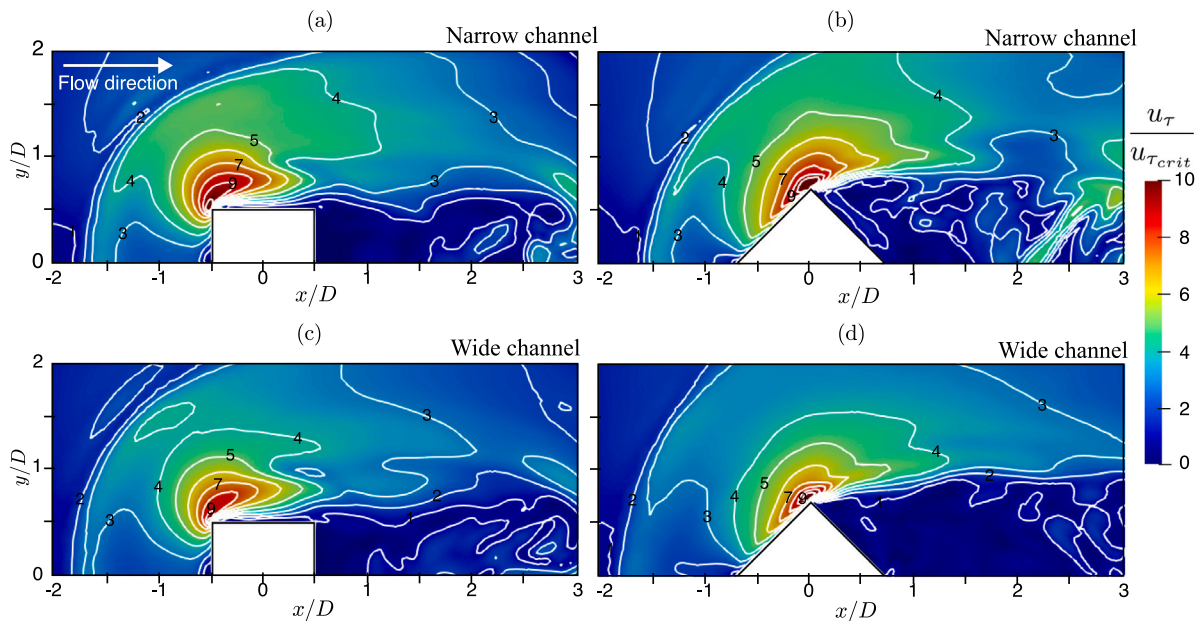

Fig. 11. Friction velocity amplification $u_\tau/u_{\tau_{crit}}$ over a rigid bed for live-bed conditions.

depending on the type of piles employed. We can also observe that there is not a significant difference in the results concerning the width of the channel.

Finally, Fig. 11 presents a similar comparison of the friction velocity amplification, but for the live-bed conditions. In contrast to the clear-water condition, the width of the channel does have a significant impact on the numerical results for the live-bed scenario. While both simulations exhibit qualitative similarities, the magnitude of $u_\tau/u_{\tau_{crit}}$ in the narrow channel is greater than in the wide case.

5.2. Scour erosion around square- and diamond-shaped piles

This section studies the morphodynamic behavior of the problem using the square- and diamond-shaped piles. A three-dimensional view of the bed topography evolution at four different stages is illustrated

in Fig. 12. These results are obtained using a narrow channel with the square-shaped pile at the two different orientations under the clear-water conditions. In the case of a square-shape pile, the scour hole is formed upstream of the obstacle since the beginning of the simulation. On the other hand, for the diamond-shape pile, the scour process initiates laterally to the obstacle, with the resulting scour hole eventually extending upstream of the pile.

Fig. 13 shows more details of the bed topography at $t/T = 2$ for the square-shaped piles under clear-water conditions. Regardless of the shape, the resulting scour hole exhibits a larger extension in the spanwise direction than in the streamwise direction. The maximum scour hole is situated at the lee-side of the square-shaped pile, near the stagnation point. Meanwhile, the maximum scour depth is found near the lateral vertices for the diamond-shaped pile. Note that the qualitative behavior of the scour hole is similar either using a narrow
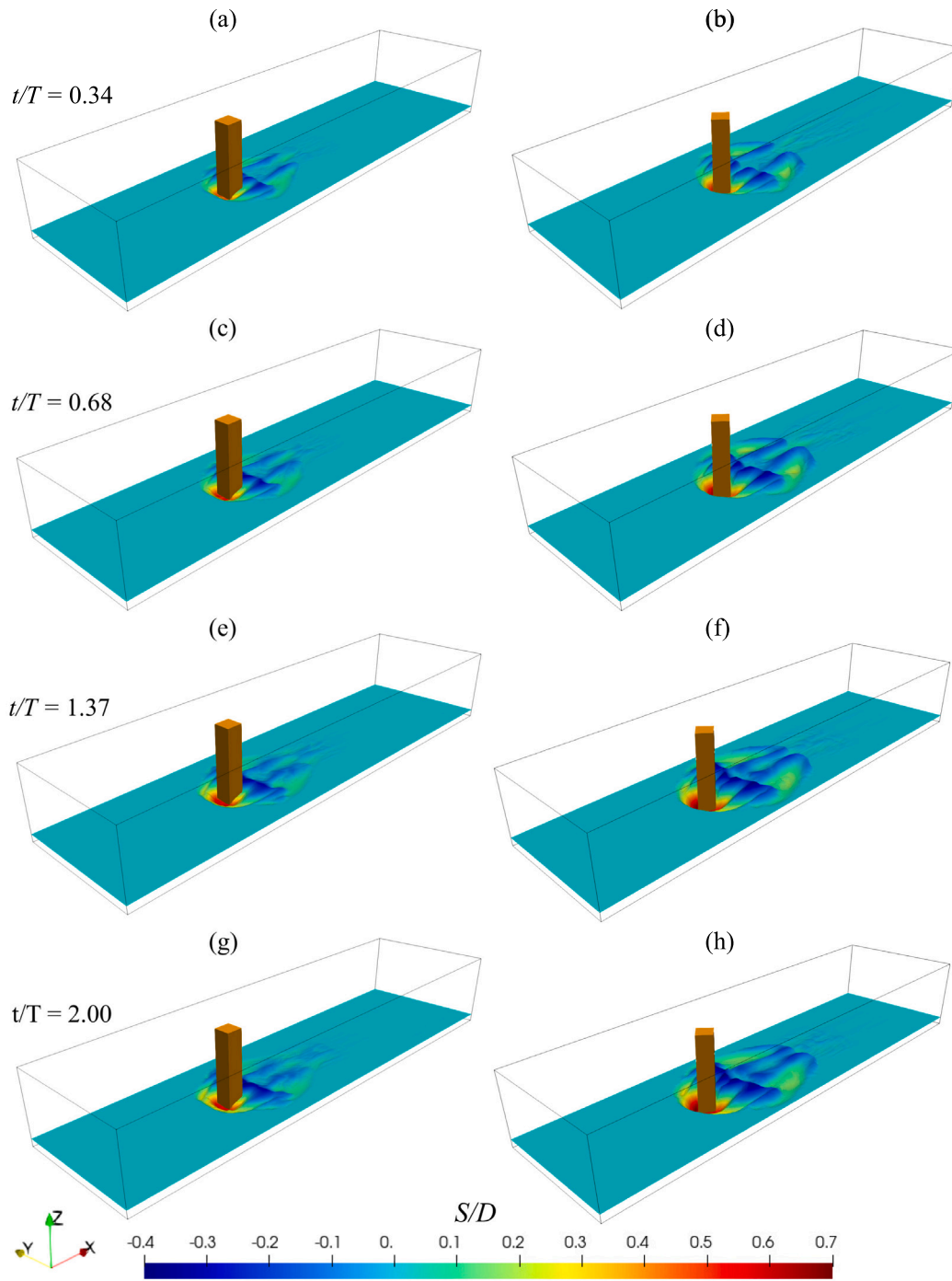
Fig. 12. Bed topography at for different stages for the narrow channel and clear-water conditions.

or a wide channel. The difference relies in their magnitude. Notably, the location of the maximum scour depth aligns with the findings of Khosronejad et al. (2012). Furthermore, it validates the selection of wide channels made by other authors (Khosronejad et al., 2012; Bordbar et al., 2021), as presented in Fig. 7.

Fig. 14 presents the bed topography at $t/T = 0.4$ under live-bed conditions. In the case of the square-shaped pile, the narrow channel exhibits a deeper scour hole and a more developed dune downstream of the pile compared to the wide configuration. Conversely, despite the difference in blockage ratio, the narrow and wide channels with a diamond-shaped pile showcase similar scour holes upstream of the pier. However, the narrow case presents a more developed scour hole

downstream of the dune, resembling the behavior observed in clear-water conditions under the same configuration.

Figs. 15(a) and (b) show the scour depth evolution in clear-water conditions, including the circular pile results. The scour depth evolution grows monotonically for all tests. However, its equilibrium stage is dependent on both the channel width and the pile shape. For the square- and diamond-shaped pile, the scour evolution is initially faster in the narrow channel than in the wide channel. However, the tendency is eventually inverted as the narrow channel cases reach equilibrium at an earlier time than the wide channel cases. This behavior can be explained by the confinement of the flow, as the flow in the narrow channel presents a velocity gradient, which weakens the flow near the side walls. Therefore the sediment transport process will also be
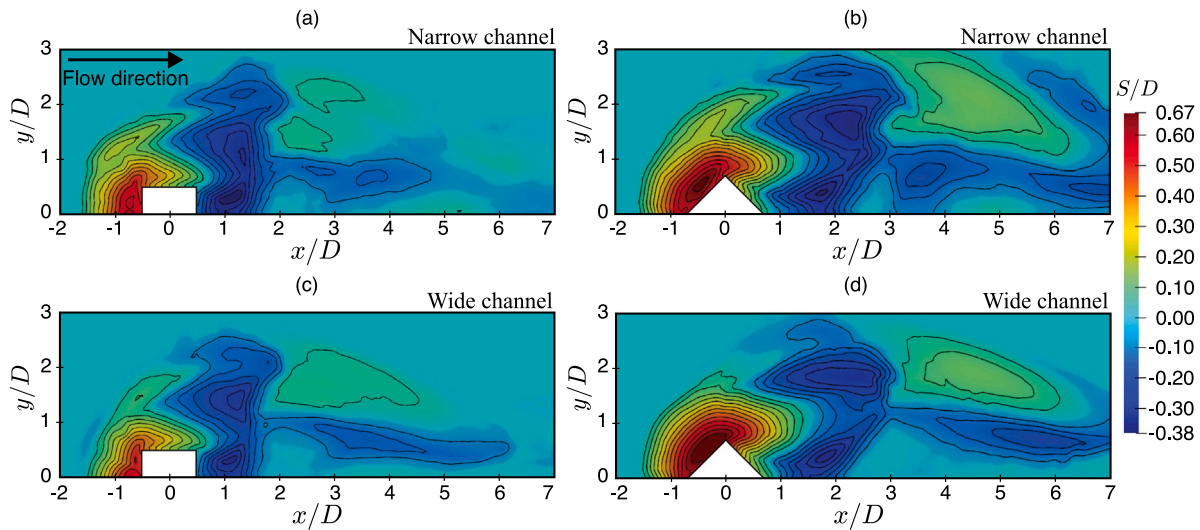
Fig. 13. Bed topography at $t/T = 2$ for the narrow and wide channel tests for clear-water conditions.
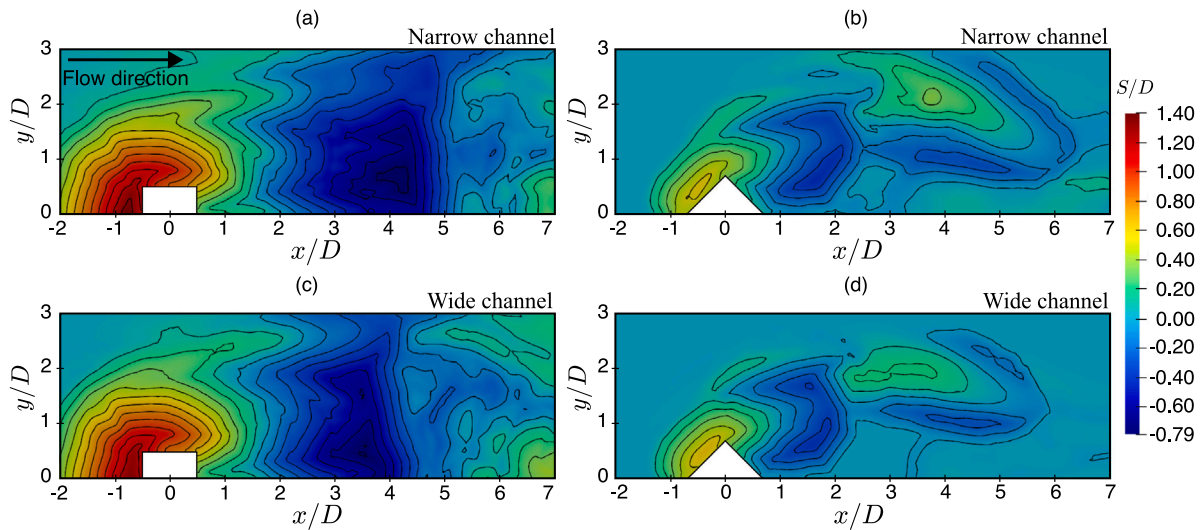

Fig. 14. Bed topography at $t/T = 0.4$ for the narrow and wide channel tests for live-bed conditions.

weakened. This behavior is consistent with the findings of Williams et al. (2019).

The time evolution for all live-bed cases is shown in Figs. 15(c) and (d). We also compared our numerical results with those presented by Bordbar et al. (2021) for live-bed conditions in a wide channel configuration. When lateral walls are present in close proximity to the pile, the displaced streamlines get hampered by the walls, which accelerates the flow lateral to the pile and creates another source of flow contraction. The narrow channel cases exhibit a faster rate of scour than their wide channel corresponding cases, but they also reach equilibrium earlier than the wide channel cases due to this effect, which both speeds up and restricts the growth of the sediment transport rate. This impact, however, was limited to clear-water scenarios since, at high velocities, the flow strength surpasses the wall effect for the selected blockage ratio $D/W = 1/8$.

In contrast to the clear-water cases, the channel width dependency of the scour depth evolution is generally weak in the live-bed cases. However, the scour depth depends strongly in the shape of the obstacle. In general, the square pier cases present the largest scour, and the diamond pier cases present the least scour. This observation is in agreement with other numerical studies, such as those by Bordbar et al. (2021) and the experimental investigations, such as the work of Xiang et al. (2020).

Concerning the square and diamond piers, it is noteworthy that the cases with the deepest and shallowest scour exhibit an inversion between clear-water and live-bed conditions, as evidenced by Fig. 15. In the clear-water regime (Fig. 15(a) and (b)) the tests with the diamond-shaped pier resulted in the deepest scour depth, consistent with experimental findings in Khosronejad et al. (2012). Conversely, in the live-bed regime (Fig. 15(c) and (d)), the tests with the square-shaped pier produced the deepest scour depth, aligning with experimental results in Yao et al. (2018). These predictions on the pile orientation which will present the more developed scour hole are independent of the blockage ratio in the cases studied in this work. As a consequence, a well designed pile (*i.e.* a streamlined shape) for live-bed can amplify the scouring during the clear water conditions and vice versa. Future work will address these results, which are not evident and require further investigation.

6. Conclusions

This paper performs an extensive numerical investigation to study the combined effects of the flow velocity conditions, channel width, and pier geometry on the scouring process in a channel with a single pile and with a bottom bed consisting of non-cohesive sediment. The aim
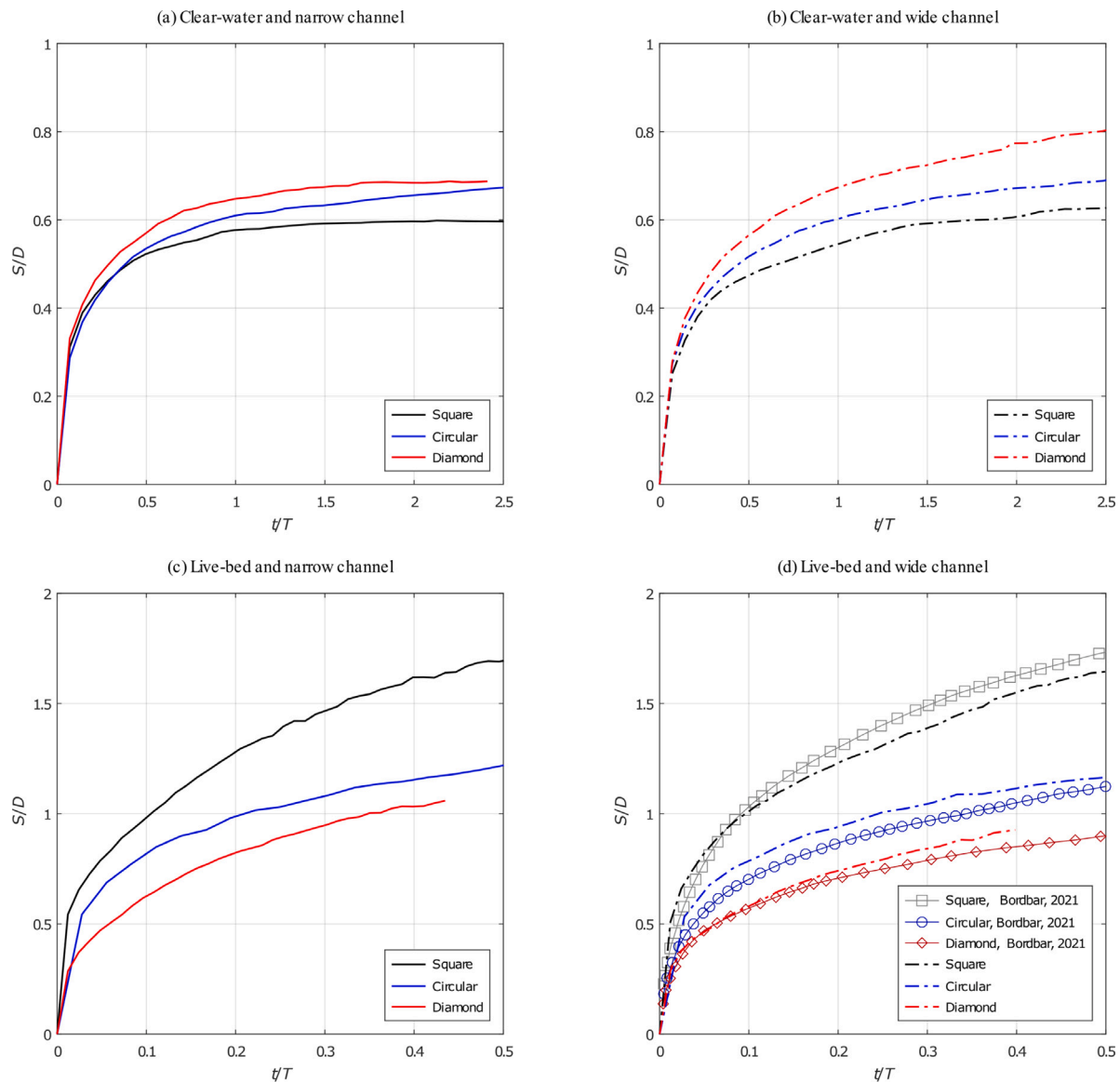
Fig. 15. Time evolution of the scour depth for different pile geometries under clear-water and live-bed conditions.

was to test the predictive capabilities of our model for a wider range of test configurations, and to use it to inquire on the impact of the flow velocity, channel width, and pile shape on the scour process.

The results presented in Section 4 demonstrate the predictive capabilities of the present model. In contrast to other models found in the literature, such as URANS (Khosronejad et al., 2012; Bordbar et al., 2021), where the maximum scour depth position tends to be misplaced for blunt piles, the present model reproduced the morphology of the scour hole particularly well. This can be explained by the fact that the LES model offers a more accurate description of the turbulence near the pile, which improves the prediction of the scour process. Furthermore, thanks to the unstructured method implemented and to the simplification of the domain by the σ-transformation, there is a fair amount of versatility with the present model for the simulation of complex shapes. The predictive capabilities of the present model are less accurate in the wake region of the domain. An explanation is that, as the ascending yet downstream of the pile induces sediment suspension, which affects the deposition pattern, the lack of a sediment suspension model limits the model's ability to accurately depict the deposition pattern. The computational cost of the current model is another possible shortcoming. It is substantially closer to a DNS model

than to a URANS model, and it restricts the length of the computational computational length to conserve computational resources.

The flow velocity seems to determine in what way the channel width and the pile geometry influence the dynamics of the scour process. Both the bluntness factor and flow velocity have an impact on how far the HSV is from the pile. The streamwise distance between the HSV and the pile increases with higher bluntness and higher velocities.

Depending on the flow velocity, the pile's geometry has opposing influences on the HSV's strength: The square-shaped pile experiences a greater flow constriction at high flow velocities than the diamond-shaped obstacle, which causes a noticeable and long-lasting rise in the scour rate. In contrast, the region of the sediment bed close to the diamond-shaped pile presents a larger friction velocity at low flow velocities, leading to a higher scour rate than the square-shaped pile case, although the difference is less significant than in the live-bed scenario. This behavior is found to be independent of the wall effect.

These results demonstrate that a pile shape optimized for a specific scour regime may not be necessarily optimal for a different regime. This behavior is particularly relevant for piles in tidal currents or during river floods. Both scour regimes may be present in these scenarios, with piles near the riverbank, usually not submerged, experiencing

clear-water conditions. At the same time, those at higher depths may encounter live-bed conditions. Future studies will aim to incorporate more complex scenarios, such as cases with multipile, cohesive sediment, or free surface conditions, and explore the corresponding influence of the Froude number. Additionally, examining the impact of roughness or investigating multi-pile configurations would be valuable considerations.

CRediT authorship contribution statement

Mario Hurtado-Herrera: Writing – original draft, Validation, Software, Methodology. **Miguel Uh Zapata:** Writing – review & editing, Supervision, Software, Methodology. **Abdelkader Hammouti:** Writing – review & editing, Supervision, Software, Methodology. **Damien Pham Van Bang:** Supervision, Software, Project administration, Methodology, Conceptualization. **Wei Zhang:** Software, Methodology, Conceptualization. **Kim Dan Nguyen:** Software, Methodology, Conceptualization.

Declaration of competing interest

The authors declare the following financial interests/personal relationships which may be considered as potential competing interests: Damien Pham Van Bang reports financial support was provided by Natural Sciences and Engineering Research Council of Canada. Damien Pham Van bang reports a relationship with Compute Canada that includes: funding grants. If there are other authors, they declare that they have no known competing financial interests or personal relationships that could have appeared to influence the work reported in this paper.

Data availability

Data will be made available on request.

Declaration of Generative AI and AI-assisted technologies in the writing process

The authors declare that no generative AI tool was used during the preparation of this work.

References

Bordbar, A., Sharifi, S., Hemida, H., 2021. Investigation of the flow behaviour and local scour around single square-shaped cylinders at different positions in live-bed. Ocean Eng. 238, 109772. http://dx.doi.org/10.1016/j.oceaneng.2021.109772.

Chen, J.H., Pritchard, W.G., Tavener, S.J., 1995. Bifurcation for flow past a cylinder between parallel planes. J. Fluid Mech. 284, 23–41. http://dx.doi.org/10.1017/S0022112095000255.

Engelund, F., Fredsøe, J., 1976. A sediment transport model for straight alluvial channels. Hydrol. Res. 7 (15), 293–306. http://dx.doi.org/10.2166/nh.1976.0019.

Fleming, J., Simpson, R., Devenport, W., 1993. An experimental study of a turbulent wingbody junction flow. Exp. Fluids 14, 366378. http://dx.doi.org/10.1007/BF00189496.

Huber, F., 1991. Update: bridge scour. ASCE 61 (9), 62–63.

Hurtado-Herrera, M., Zhang, W., Hammouti, A., Pham Van Bang, D., Nguyen, K.D., 2023. Numerical study of the flow and blockage ratio of cylindrical pier local scour. Appl. Sci. 13 (11501), http://dx.doi.org/10.3390/app132011501.

Khosronejad, A., Flora, K., Sotiropoulos, F., 2012. Experimental and computational investigation of local scour around bridge piers. Water Resour. 37 (Sep), 73–85. http://dx.doi.org/10.1016/j.advwatres.2011.09.013.

Lachaussée, F., 2018. Érosion et transport de particules au voisinage d'un obstacle (in French) (Ph.D. thesis). Paris Fr, https://www.theses.fr/2018SACLS377.

Lachaussée, F., Bertho, Y., Morize, C., Sauret, A., Gondret, P., 2018. Competitive dynamics of two erosion patterns around a cylinder. Phys. Rev. Fluids 3 (1), http://dx.doi.org/10.1103/PhysRevFluids.3.012302.

Lin, C., Han, J., Bennett, C., Parsons, R.L., 2014. Case history analysis of bridge failures due to scour. Clim. Eff. Pavement Geotech. Infrastructure 20, 4–216. http://dx.doi.org/10.1061/9780784413326.021.

Mason, P.J., Thomson, D.J., 1992. Stochastic backscatter in large-eddy simulations of boundary layers. J. Fluid Mech. 242 (1), 51. http://dx.doi.org/10.1017/S0022112070000691.

Melville, B.W., Chiew, Y.M., 1999. Time scale for local scour at bridge piers. J. Hydraul. Eng. 125, 59–65. http://dx.doi.org/10.1061/(ASCE)0733-9429(1999)125:1(59).

Mignot, E., Moyne, T., Doppler, D., Riviere, N., 2015. Clear-water scouring process in a flow in supercritical regime. J. Hydraul. Eng. 142 (4), http://dx.doi.org/10.1061/(ASCE)HY.1943-7900.0001100.

Nikuradse, J., 1933. Laws of flow in rough pipes. NACA TM 1292.

Raudkivi, A., Ettema, R., 1983. Clear-water scour at cylindrical piers. J. Hydraul. Eng. 109 (3), 338–350.

Roulund, A., Sumer, B.M., Fredsøe, J., Michelsen, J., 2005. Numerical and experimental investigation of flow and scour around a circular pile. J. Fluid Mech. 534, 351–401. http://dx.doi.org/10.1017/S0022112005004507.

Simpson, R.L., 1995. Some aspects of three-dimensional turbulent separation. In: Twelfth Australasian Fluid Mechanics Conference. The University of Sydney, Australia.

Singha, S., Sinhamahapatra, K.P., 2010. Flow past a circular cylinder between parallel walls at low reynolds numbers. Ocean Eng. 37, 757–769. http://dx.doi.org/10.1016/j.oceaneng.2010.02.012.

Soulsby, R., 1997. Dynamics of Marine Sands: A Manual for Practical Applications. Thomas Telford, London UK.

Soulsby, R., Whitehouse, R., 1997. Threshold of sediment motion in coastal environments. In: Proceedings of the 13th Australasian Coastal and Ocean Engineering Conference and the 6th Australasian Port and Harbour Conference, vol. 1, p. 145, https://search.informit.org/doi/10.3316/informit.929741720399033.

Stevens, M.A., Gasser, M.M., Saad, M.B.A.M., 1991. Wake vortex scour at bridge piers. J. Hydraul. Eng. 117 (7), 891–904. http://dx.doi.org/10.1061/(ASCE)0733-9429(1991)117:7(891).

Sumer, B., Fredsøe, J., Christiansen, N., 1992. Scour around vertical pile in waves. J. Waterw., Port, Coast., Ocean Eng. 118 (1), 15–31. http://dx.doi.org/10.1061/(ASCE)0733-950X(1992)118:1(15).

Swamee, P.K., 1993. Generalized inner region velocity distribution equation. J. Hydr. Eng. 119 (5), 651–656. http://dx.doi.org/10.1061/(ASCE)0733-9429(1993)119:5(651).

Taricska, M., 2014. An Analysis of Recent Bridge Failures (2000–2012) (Master's thesis). Ohio US.

Uh Zapata, M., Hernandez-Lopez, F.J., Itzá Balam, R., 2023. A parallel unstructured multi-color sor solver for 3D navier–stokes equations on graphics processing units. Comput. & Fluids 260, 105909. http://dx.doi.org/10.1016/j.compfluid.2023.105909.

Uh Zapata, M.A., Pham Van Bang, D., 2016. Parallel sor methods with a parabolic-diffusion acceleration technique for solving unstructured-grid Poisson equation on 3D arbitrary geometries. Int. J. Comput. Fluid Dyn. 30 (5), 370–385. http://dx.doi.org/10.1080/10618562.2016.1234045.

Uh Zapata, M., Pham Van Bang, D., Nguyen, K.D., 2014. An unstructured finite volume technique for the 3D Poisson equation on arbitrary geometry using a sigma-coordinate system. Internat. J. Numer. Methods Fluids 76 (10), 611–631. http://dx.doi.org/10.1002/fld.3945.

Wardhana, K., Hadipriono, F.C., 2003. Analysis of recent bridge failures in the united states. J. Perform. Constr. Facil. 17 (3), 144–150. http://dx.doi.org/10.1061/(ASCE)0887-3828(2003)17:3(144).

Williams, P., Balachandar, R., Bolisetti, T., 2019. Examination of blockage effects on the progression of local scour around a circular cylinder. Water 11 (2631), http://dx.doi.org/10.3390/w11122631.

Xiang, Q., Wei, K., Qiu, F., Yao, C., Li, Y., 2020. Experimental study of local scour around caissons under unidirectional and tidal currents. Water 12 (640), http://dx.doi.org/10.3390/w12030640.

Yao, W., An, H., Draper, S., Cheng, L., Harris, J.M., 2018. Experimental investigation of local scour around submerged piles in steady current. Coast. Eng. 142, 27–41. http://dx.doi.org/10.1016/j.coastaleng.2018.08.015.

Zapata, M.Uh., Zhang, W., Pham Van Bang, D., Nguyen, K.D., 2019. A parallel second-order unstructured finite volume method for 3D free-surface flows using a σ coordinate. Comput. & Fluids 190, 15–29. http://dx.doi.org/10.1016/j.compfluid.2019.06.001.

Zhang, W., Uh Zapata, M., Bai, X., Pham Van Bang, D., Nguyen, K.D., 2020b. An unstructured finite volume method based on the projection method combined momentum interpolation with a central scheme for three-dimensional nonhydrostatic turbulent flows. Eur. J. Mech. / B Fluids 84, 164–185. http://dx.doi.org/10.1016/j.euromechflu.2020.06.006.

Zhang, W., Zapata, M.Uh., Bai, X., Pham Van Bang, D., Nguyen, K.D., 2020a. Three-dimensional simulation of horseshoe vortex and local scour around a vertical cylinder using an unstructured finite-volume technique. Int. J. Sediment Res. 35 (3), 295–306. http://dx.doi.org/10.1016/j.ijsrc.2019.09.001.